

Alma Mater Studiorum Università di Bologna  
Archivio istituzionale della ricerca

On the origin of controlled anisotropic growth of monodisperse gold nanobipyramids

This is the final peer-reviewed author's accepted manuscript (postprint) of the following publication:

*Published Version:*

Meena S.K., Lerouge F., Baldeck P., Andraud C., Garavelli M., Parola S., et al. (2021). On the origin of controlled anisotropic growth of monodisperse gold nanobipyramids. NANOSCALE, 13, 15292-15300 [10.1039/d1nr01768c].

*Availability:*

This version is available at: <https://hdl.handle.net/11585/845931> since: 2023-02-28

*Published:*

DOI: <http://doi.org/10.1039/d1nr01768c>

*Terms of use:*

Some rights reserved. The terms and conditions for the reuse of this version of the manuscript are specified in the publishing policy. For all terms of use and more information see the publisher's website.

This item was downloaded from IRIS Università di Bologna (<https://cris.unibo.it/>).  
When citing, please refer to the published version.

(Article begins on next page)

Cite this: DOI: 00.0000/xxxxxxxxxx

# On the Origin of Controlled Anisotropic Growth of Monodisperse Gold Nanobipyramids<sup>†</sup>

Santosh Kumar Meena,<sup>\*a</sup> Frederic Lerouge,<sup>b</sup> Patrice Baldeck,<sup>b</sup> Marco Garavelli,<sup>c</sup> Stephane Parola,<sup>b</sup> Marialore Sulpizi,<sup>\*d</sup> and Ivan Rivalta<sup>\*cb</sup>

Received Date

Accepted Date

DOI: 00.0000/xxxxxxxxxx

We elucidate the crucial role of the cetyl trimethylammonium bromide (CTAB) surfactant in the anisotropic growth mechanism of gold nano-bipyramids, nano-objects with remarkable optical properties and high tunability. Atomistic molecular dynamics simulations predict different surface coverages of the CTAB (positively charged) heads and their (bromide) counterions as function of the gold exposed surfaces. High concentration of CTAB surfactant promotes formation of gold nanograins in solution that work as precursors for the smooth anisotropic growth of more elongated nano-bipyramidal objects. Nanobipyramids feature higher index facets with respect to nanorods, allowing higher CTAB coverages that stabilize their formation and leading to narrower inter-micelles channels that smooth down their anisotropic growth. Absorption spectroscopy and scanning electron microscopy confirmed the formation of nanograins and demonstrated the importance of surfactant concentration on driving the growth towards nano-bipyramids rather than nanorods. The outcome explains the formation of the monodisperse bipyramidal nano-objects, the origin of their controlled shapes and sizes along with their remarkable stability.

## 0.1 Introduction

Gold nanoparticles with bipyramidal structure feature high field enhancement, especially near their tips, with respect to gold nanorods, making these nano-objects promising candidates for sensing applications involving enhanced Raman and fluorescence spectroscopy techniques<sup>1,2</sup>. The plasmon resonance spectral range and the optical enhancement can be tuned through shape and size of gold nanobipyramids (GNBs). However, full control of shape and size during the growth is challenging since the aspect ratio (AR) of the final nano-object depends on various factors including initial seed crystalline phase, surfactant type, reducing agent and other additives such as silver ions in growth solution<sup>3–5</sup>. For widespread application of these engineered nano-objects, fine control of the AR of GNBs (shape and size) has to be accompanied by monodispersity, i.e. the homogeneity of the

nanoparticles morphology<sup>6</sup>. Purified monodispersed bipyramids can be indeed used as seed for regrowing a variety of bipyramid-based nanoparticles with intriguing properties<sup>6</sup>.

In contrast to the seed-mediated synthesis of nanorods from single crystal or (with low yield) multi-twinned seeds, bipyramidal nanoparticles are synthesized using multi-twinned nanograin seeds produced in citrate solution and in presence of silver(I) salt starting from penta-twinned gold seeds<sup>3,5</sup> (see Figure 1a). Analysis of high-resolution transmission electron microscopy (TEM) images and their powder spectrum revealed that gold bipyramids produced with seed-mediated growth techniques in presence of silver ions and cetyl trimethylammonium bromide (CTAB) surfactant have penta-fold twinning structure<sup>3,6–10</sup>. Burgin et al. and Yoo et al. have reported 6-fold twinning structure with silver(I)-assisted growth using cetyltrimethylammonium chloride (CTAC) and salicylic acid as surfactants<sup>11,12</sup>. Here, we consider the more common penta-fold base nano-bipyramids. The structural model of nanograins based on TEM analysis<sup>5</sup> suggests a bipyramidal shape with small AR (1.25–1.83), lateral (100) facets, (110)-truncated (111) tips and bridging, minimally stepped higher index (112) facets, see Figure 1a. In order to fit the bipyramidal geometry, in fact, the lateral (100) facets (typical of nanorods) have to be stepped periodically along the growth direction averaging out to (11 $\bar{l}$ ) facets, with  $\bar{l}$  increasing with the ideal AR of

<sup>a</sup> Chemical Engineering and Process Development Division, CSIR-National Chemical Laboratory (NCL), Dr. Homi Bhabha Road, Pune-411008, India, Fax: +91 20 2590 2612; Tel: +91 20 2590 2468; E-mail: sk.meena@ncl.res.in

<sup>b</sup> Univ Lyon, Ens de Lyon, CNRS UMR 5182, Université Claude Bernard Lyon 1, Laboratoire de Chimie, F69342, Lyon, France.

<sup>c</sup> Dipartimento di Chimica Industriale "Toso Montanari", Università degli Studi di Bologna, Viale del Risorgimento 4, I-40136 Bologna, Italy.; E-mail: ivan.rivalta@ens-lyon.fr

<sup>d</sup> Institute of Physics, Johannes Gutenberg University Mainz, Staudingerweg 7, 55099 Mainz, Germany. E-mail: sulpizi@uni-mainz.de;

<sup>†</sup> Electronic Supplementary Information (ESI) available: [details of any supplementary information available should be included here]. See DOI: 00.0000/00000000.

**Table 1** Properties of bipyramidal objects, including ideal aspect ratio (AR), step size and cone angle associated to the exposed lateral surface.

Lateral surface	Ideal AR	Step size	Cone angle [ $\theta^\circ$ ]
Au (111)	0.71	0.5	120
Au(112)	1.41	1	81.79
Au(113)	2.12	1.5	60
Au(114)	2.83	2	46.83
Au(115)	3.54	2.5	38.54
Au(116)	4.24	3	32.20
Au(117)	4.95	3.5	27.80

the GNBs (see Figure 1)<sup>6</sup>. Gold bipyramids feature characteristic truncated, generally smooth tips in contrast to multi-twinned seeds and nanorods tips with Au(111) exposed surfaces and cone angle of  $\theta = 120^\circ$ . The cone angle of an ideal (i.e. non-truncated) bipyramid correlates with its ideal AR and it decreases with the  $l$  index of lateral (11 $l$ ) facets (see Figure 1).<sup>5,6</sup> Cone angles, Miller indices and step sizes of the side surfaces and AR of ideal bipyramids are reported in Table 1, as determined by using the relation introduced by Lee et. al<sup>6</sup>.

It is established that the generation of anisotropic nanograins and the subsequent use of silver(I) salt are crucial for the anisotropic growth of GNBs<sup>3,5</sup>, but the role of surfactant coverage on the stabilization of nanograins still remains elusive as well as the origin of their anisotropic growth into bipyramids (with surprisingly stable high-index stepped surfaces) instead of nanorods (with low-index flat surfaces). Recently, Gonzalez-Rubio et al. have showed that lower CTAB concentration and lower reactant concentration at lower temperature produce nanorods whereas higher CTAB concentration in growth solution results into GNBs<sup>13</sup>. Still, mechanism behind CTAB concentration dependent morphological change has not been investigated so far and it's not clear why does higher CTAB concentration result into GNBs knowing the fact that gold nanorods are more thermodynamically stable than GNBs.

Density functional theory (DFT) calculations have been used to analyze the absorption of surfactant molecules, bromide and silver ions on gold surfaces, providing insights on the growth mechanism of gold nanorods<sup>14</sup>. The high cost of static DFT calculations limits the model size, making the inclusion of solvent and dynamics effects challenging, if not prohibitive, at this level of theory. Classical molecular dynamics (MD) simulations are of fundamental importance for realistic modeling of the complex gold nanoparticles interfaces. Such atomistic simulations showed to be particularly useful for understanding the origin of the asymmetric growth mechanism in gold nanorods<sup>15–17</sup>. In particular, we used MD simulations to study the different factors influencing the nanorods growth, unraveling the role of the CTAB surfactant head groups<sup>15</sup> and their counterions (bromide, chloride<sup>17</sup> along with the importance of silver ions<sup>16</sup>) and initial seed geometry<sup>16</sup>. Nanoseed models<sup>16</sup> in the size of a few nanometers and (infinite) surface models<sup>15,17</sup>, the later representing the final stage of the nanorods side facets, have been employed to compute surface coverage of ions and molecules, structural properties of absorbed surfactant moieties and diffusion of physisorbed species from long (0.2–0.3 microseconds) MD simulations. We showed that CTAB formed distorted cylindrical micelles separated by water-ion channels on low-index (e.g. 111, 110, and 100) gold surfaces, which can provide a path for the diffusion of ions and Au reactants towards the gold surfaces. Au(100) and Au(110) surfaces shows higher CTAB

coverage and narrower water-ion channels than Au(111), demonstrating the presence of surface-dependent coverage of surfactant and ions.<sup>15</sup> Such preferential coverage is even more pronounced on penta-twinned decahedral and cuboctahedral seeds and small nanorods models, indicating symmetry breaking in the initial seeds and explaining the anisotropic growth of nanorods.<sup>16</sup> Finally, MD simulations including silver ions, which are known for improving the yield of anisotropic particles, indicated that the structure of the CTAB micellar layer is not qualitatively modified by the silver salt addition while the anisotropic surface coverages are slightly enhanced, resulting into an increased surface passivation and more efficient anisotropic growth.

A polarizable model for gold atoms that includes image charges has been employed for peptides binding on Au(111) surface, showing that polarization of gold atoms contributes for 10–20% of the binding energy<sup>18</sup>. While a generalization of such polarization effect on the binding of large molecular systems, such the CTAB micelles investigated here, is not yet available, we have recently developed an approach to quantitatively include image charges on gold surfaces<sup>19</sup>, suggesting that image charges will not play a major role on planar surfaces. Thus, we employed here a non-polarizable model to study the CTAB coverage effects on planar surfaces, being aware that polarization of gold atoms may have some non-trivial effects at the edges/tips of GNBs, which are beyond the scope of this work. Moreover, this simulation protocol has been previously validated by comparison with experimental studies investigating the role of halide ions<sup>17</sup> in controlling the nanorods growth mechanism from penta-twinned nanoseeds,<sup>16</sup> and it will be conveniently used here to provide a direct comparison between various nano-objects. Here, we performed such simulations in conjunction with experimental studies involving the preparation of GNBs from seeds added in growth solution containing various concentrations of CTAB, revealing the origin of selective anisotropic growth of gold seeds to nano-bipyramidal objects. The experiments consisted in monitoring the growth of GNBs with UV/visible spectroscopy just after addition of the seeds within the growth solution and recording SEM images of the produced nano-objects. The outcome provides explanation for the experimentally observed large monodispersity of synthetic GNBs with high-index (stepped) exposed surfaces, which form more favorably than nanorods featuring low-index (flat) facets.

## 0.2 Models and Simulation Details

Model details of the nanograin systems in the absence and presence of silver ions are reported in Table 2. Nanograin model with real AR=1.6 and ideal AR=1.56 consist (112) bridging facets, (111) and (110) facets on the tip and (100) on the side as shown in Figure 1a. Nanograin first covered with CTA<sup>+</sup> and then solvated with water molecules. Bromide ions (Br<sup>-</sup>) were added by randomly replacing water molecules. For the simulation model in the presence of silver ions, silver ions were added by randomly replacing the water molecules in the system of nanograin surrounded with CTA<sup>+</sup>, Br<sup>-</sup> and solvated with water molecules. A number of extra Br<sup>-</sup> were also added to naturalize silver ions (Table 2).

In Table 3, details of the Au/CTAB/water model systems for the different types of high-index surfaces are reported. Our models for the higher index facets of GNBs consist of a gold higher index slab in contact with a CTAB bilayer and electrolyte solution. The preassembled system with of CTA<sup>+</sup> surfactants on gold slab was, first solvated with water in a simulation box and subsequently Br<sup>-</sup> were added to the system by randomly replacing them with water molecules.

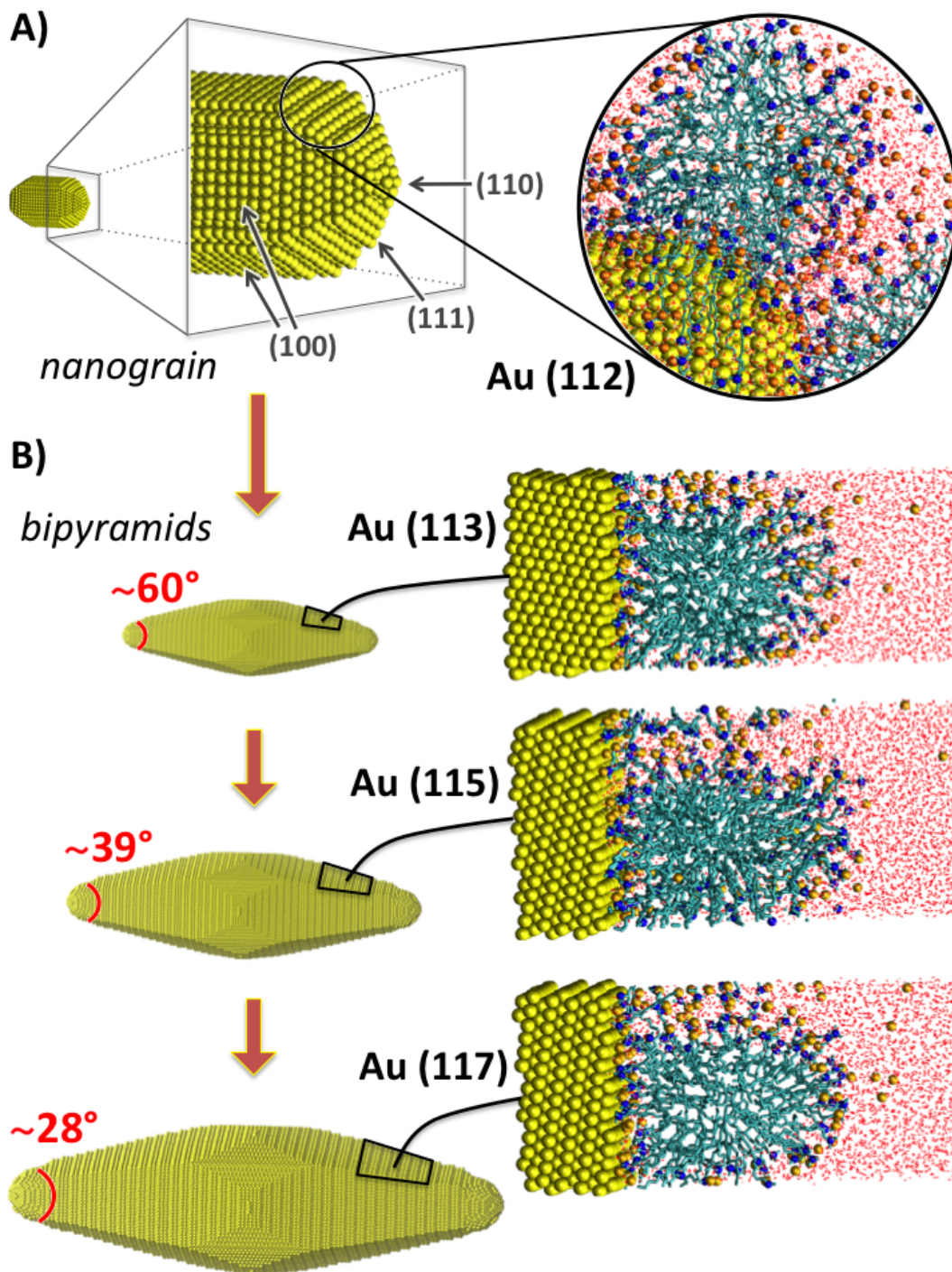


**Fig. 1** (A) Atomistic models of a nanograin with real AR = 1.6 and ideal AR = 1.56, which matches the experimentally observed structure<sup>5</sup> and structure of a CTAB micelle on the (112) facet of nanograin after 0.5  $\mu$ s simulation run. (B) Growth of bipyramidal nanoparticles from a nanograin, including GNBs with Au(113) side facets and cone angle  $\theta \sim 60^\circ$ , (115) side facets and  $\theta \sim 39^\circ$  and (117) side facets and  $\theta \sim 28^\circ$ . Structures of CTAB micelles in water on Au(113), Au(115), Au(117) surfaces obtained from MD simulations after 0.5  $\mu$ s.



**Table 2** Model details of the nanograin systems in the absence and presence of silver ions.

Name of system	Without Ag <sup>+</sup>	With Ag <sup>+</sup>
No. of Au Atoms	5220	5220
No. of CTAB molecules	2400	2400
No. of AgBr	0	480
No. of of water molecules	83381	82421
Box dimensions X [nm], Y [nm] Z [nm]	15.45, 15.45, 16.48	15.46 15.46 16.49

**Table 3** Model details for CTAB in aqueous solution on Au(113), Au(115) and Au(117) surfaces.

Name of surface	No. of CTAB molecules	No. of water molecules	Thickness of gold surface [nm]	Box dimensions X [nm], Y [nm] Z [nm]
Au (113)	180	4884	2.13	4.09, 4.09, 16.06
Au (115)	212	6525	1.83	4.49, 4.49, 16.10
Au (117)	180	4884	1.90	4.09, 4.09, 15.88

All MD simulations have been performed using the GROMACS package (version 2016.4)<sup>20–23</sup>. Periodic boundary conditions were applied in all three directions. Energy minimization was performed after the addition of water and ions to keep the maximum force on any atom below  $1000 \text{ kJmol}^{-1}\text{nm}^{-1}$ . A constant temperature of 300 K and a constant pressure of 1 bar were maintained by using the Berendsen thermostat and Parrinello-Rahman barostat, as implemented in GROMACS. A time step of 2 fs was employed and trajectories were stored at every 2 ps. In a typical simulation, the system was first equilibrated in the NVT ensemble for 100 ps, NPT ensemble for 100 ps. After pre-equilibration, MD production runs were performed for at least for 500 ns in NPT ensemble, as showed in Figure S1 in the supporting information. Trajectories from the last 100 ns were used for analysis.

GROMOS96 53a6 forcefield<sup>24</sup> was employed for all our MD simulations, in line with our previous work<sup>15–17</sup>. In particular, the cetyltrimethylammonium cation (CTA<sup>+</sup>) model proposed and validated by Wang and Larson<sup>25</sup> has been used in combination with the SPC water model. The charge assignment for CTA<sup>+</sup> is such that the three methyl groups in the head group and the methylene group adjacent to the nitrogen carry a partial positive point charge of + 0.25e each and the central nitrogen atom is set to be neutral<sup>25</sup>. The Lennard-Jones parameters for bromide ion and gold are taken from Van-Gunsteren et al.<sup>26</sup> and Heinz et al.<sup>27</sup>, respectively.

### 0.3 Experimental details

The gold nanobipyramids were prepared following a seed mediated growth process already described elsewhere<sup>8</sup>. The two-step approach focuses on first the design of multitwinned seeds followed by their addition in a growth solution.

#### 0.3.1 Preparation of the seeds

Briefly, the seeds were prepared by reduction of a gold salt (HAuCl<sub>4</sub> – 0.5 mM) with a quick addition of a NaBH<sub>4</sub>/NaOH mixture in water (50 mM of NaBH<sub>4</sub> and 50 mM of NaOH) in presence of surfactant (CTAC – 95 mM) at 20°C. The mixture was then aged by heating at 85°C during 1 hour. Preparation of the growth solutions. The growth solution was prepared first by mixing 40 l of gold salt (HAuCl<sub>4</sub> – 0.025 M in water) with a 4ml CTAB solution in water (0.045 M or 0.022M). Then, silver nitrate (18 l – 0.01 M in water) and of 8-hydroxyquinoline (50 L – 0.4M in ethanol) were added.

#### 0.3.2 Preparation of the GNBs

40 l of gold seeds suspension were added in the 0.045M CTAB growth solution or in the 0.022M CTAB growth solution. After quick stirring for homogenization the mixture was placed in a cuvette in a UV/Vis spectrometer for GNBs growth monitoring.

UV-vis experiments were performed in suspension in water, on a Perkin Elmer Lambda750, with double-cuvette chamber. Electronic microscopy was performed on a scanning electron microscope Zeiss Supra 55 VP ( vacuum 5.10-6 mbars, tension : 10kV).

### 0.4 Results and Discussion

In this work, we have considered Au(11*l*) surfaces with *l*=1, 3, 5, and 7, thus ranging from the planar surface that models nanorod tips (with Au(111) surface and  $\theta = 120^\circ$ ) to the stepped Au(117) surface of largely elongated GNBs, featuring ideal AR~5 and  $\theta \sim 27.8^\circ$ . It is worth noting that while the truncation of bipyramid tips can significantly modify the AR of the nanoparticle, reducing the ideal AR to a smaller "real" AR, tip truncation does not affect the cone angle and consequently the step size of the high-index surface of the GNBs, see Table 1. Multi-twinned gold seeds favor the anisotropic growth of elongated objects (such as nanorods and nano-bipyramids) due the low surface density at their Au(111) tips.<sup>16</sup> Previous MD simulations, indeed, indicated that the CTA<sup>+</sup> and the Br<sup>-</sup> surface densities of 1.31 and 1.09 ions/nm<sup>2</sup> for heads and ions, respectively, on clean Au(111) surfaces are drastically reduced to 0.19 and 0.30 ions/nm<sup>2</sup>, respectively, on penta-twinned seeds tips. As the growth progresses on the nanoseeds Au (111) tips, the  $\theta = 120^\circ$  cone angle reduces and the real AR of the object increases to 1.25-1.83, finally forming a nanograin<sup>5</sup>. An ideal bipyramid with  $\theta = 81.79^\circ$  and (112) facets on sides has an ideal AR=1.41, see Table 1, which falls in the range of the real AR measured for nanograins.<sup>5</sup> The TEM-based structural model of nanograin, in fact, features bridging (112) facets, with a real AR of 1.56 and a similar ideal AR (i.e. 1.60), as the truncation percentage in these objects appears to be minimal.<sup>5</sup>

Therefore, we have first computed the surface densities for the exposed surfaces of a nanograin realistic model (Figure 1a), based on the structure proposed by Canbek et al.<sup>5</sup>. We employed the GROMACS package (version 2016.4)<sup>20–23</sup> and previously reported forcefields<sup>15–17,25–27</sup>. As reported in Table 4, the less covered surface on the nanograins is the (111), with surfactant molecules density of ~0.9 ions/nm<sup>2</sup>, while the most dense of CTA<sup>+</sup> ions is the (100), with ~1.6 ions/nm<sup>2</sup>, with the (112) and (110) showing

similar densities 1.3-1.4 ions/nm<sup>2</sup>. These surface coverage values explain why the growth of nanograins occurs predominantly at the (111) bridges, consistently with an anisotropic elongation towards bipyramidal objects featuring lateral surfaces with indexes higher than (112), i.e. (111) with  $l \geq 3$ , see (Figure 1). This trend is conserved if silver salt (AgBr) is added, as reported in Table S1 in the supporting information, addition of silver ions increased the surface density of CTA<sup>+</sup> and Br<sup>-</sup> ions on (111), (112) and (100), remained higher on (112) and (100) than (111) and (110). Surface density of silver ions is found to be higher on (100) and (112) facets than (111) and (110) facets of nanograin (see Table S1 in the Supporting Information). The total ion density (sum of densities of all the ions) increased on all the facets due to the addition of silver ions with the conservation of similar anisotropic coverage as observed in the absence of silver ions but with higher surface densities (see Table S2 in Supporting Information). The anisotropic coverage of silver ions together with anisotropic coverage with higher surface densities CTA<sup>+</sup> and Br<sup>-</sup> ions on the different facets of nanograin as compare to the absence of silver ions lead to controlled anisotropic growth of nanobypiramids. Notably, the CTA<sup>+</sup> density on the (111) bridge of nanograins (in presence or absence of silver ions) is significantly larger than that on the (111) tips of penta-twinned nanoseeds, 0.19 ions/nm<sup>2</sup>.<sup>16</sup> This difference suggests that, in presence of large CTAB concentrations, a fast anisotropic growth of penta-twinned nanoseeds toward nanograins has to be expected, followed by stabilization of the (112) bridge facets (featuring large surface CTAB coverage) and appearance of (111) nanograin bridges with intermediate surfactant coverage, which can still accommodate gold atoms for further growth toward GNBs. Overall, these results indicate that the concentration of CTAB surfactant molecules is a crucial factor that could regulate the role of nanograins as GNBs precursors.

**Table 4** Surface density of CTA<sup>+</sup> and Br<sup>-</sup> on different facets of nanograin. The standard error is given in small brackets.

Name of surface	CTA <sup>+</sup> /nm <sup>2</sup>	Br <sup>-</sup> /nm <sup>2</sup>
Au(110)	1.31 (0.60)	1.30 (0.56)
Au(111)	0.87 (0.21)	0.36 (0.16)
Au(112)	1.40 (0.06)	1.35 (0.07)
Au(100)	1.64 (0.05)	1.63 (0.05)

As showed in Figure 2A-B, the effect of CTAB surfactant molecules concentration on the the seed-mediated growth process (see ref<sup>8</sup> for experimental details) has been monitored by UV-vis spectroscopy for concentrations at 0.045M and 0.022M of CTAB, following the evolution of the localized surface plasmon resonance (LSPR) bands during time. At the very early stages, i.e. few seconds upon addition of gold seeds to the growth solution, the recorded UV-vis spectra feature noticeable differences as function of the CTAB concentration. At CTAB 0.045 M, the characteristic LSPR signal of nanograins, right below 550 nm<sup>5</sup>, is clearly detected immediately after seeds addition, in agreement with the fast anisotropic nanoseeds-to-nanograins growth predicted by our MD simulations. In contrast, at lower surfactant concentration, a quite broad absorption signal is observed between 500 and 550 nm together with a more intense band above 600 nm, indicating a rapid formation of elongated and poly-disperse objects in the growth solution at early stages. As showed in Figure 2A, high CTAB concentration allows smooth conversion of the nanograins into GNBs in 1-2 minutes, featuring typical lateral LSPR band at ~520 nm and longitudinal bands above 600 nm, red-shifting with time by following the elongation of the bipyramidal object. Notably, halv-

ing the CTAB concentration (to 0.022 M) has a dramatic effect on the UV-vis spectra, with quite broad absorption bands appearing between 500-600 nm and longitudinal LSPR signals being significantly red-shifted above 700 nm, see Figure 2B. The time evolution of the UV-vis spectra clearly indicates that reducing the amount of CTAB in the growth solution causes loss of monodispersity (LSPR broadening) and acceleration of the (uncontrolled) growth (fast red-shift).

Scanning electronic microscopy (SEM) was performed on the final products obtained by the seed-mediated growth synthesis with 0.045 M and 0.022 M CTAB, in order to confirm the effect of surfactant concentration on the size and morphology of the resulting nano-objects. As showed in Figure 2C, GNBs with longitudinal sizes in the 90-100 nm range are obtained in high yield (85 %) with high CTAB concentration and only few byproducts are observed as spheres. If the CTAB concentration is lowered to 0.022 M, see Figure 2D, more elongated (110 nm) and distorted bipyramids are obtained in a low yield (55%), accompanied by formation of small nanorods (with average length of 20 nm and small AR of 1.4-1.6) and few spheres. Thus, the increase of surfactant concentration induces stabilization of GNBs growth possessing high-index (111) stepped facets and in absence of enough CTAB molecules the control on the size and morphology is lost with the formation of small nanorods, with exposed (100) surfaces.

In order to disclose the origin of the stability of high-index (111) facets forming at the sides of GNBs during the growth mechanism at high surfactant concentration, we have simulated the CTAB adsorption in aqueous medium on the Au(113), Au(115) and Au(117) stepped surfaces (see Figure 1B) and compared them with previous analysis of nanorods (100) surfaces.<sup>15</sup> The extended (111) surfaces are used to model the side facets of GNBs with ideal AR of ~2.1, ~3.5 and ~4.9, respectively. In Table 5, we report the average CTAB surface densities and inter-micelles channels widths for these surfaces, as computed from long MD simulations (ca. 0.5  $\mu$ s) (see Figure S1 in Supporting Information). CTAB molecules form micellar structure on the stepped surfaces with surface densities of 1.58, 1.51 and 1.59 CTA<sup>+</sup>/nm<sup>2</sup> and 1.53, 1.60 and 1.61 Br<sup>-</sup>/nm<sup>2</sup> on Au(113), Au(115) and Au(117), respectively (Table 5). These surface densities of CTA<sup>+</sup> and Br<sup>-</sup> ions are higher than those found for flat surfaces with lower index facets Au(111), Au(110) and Au(100), reported to be <1.50 ion/nm<sup>2</sup>.<sup>16</sup>

**Table 5** Surface density of CTA<sup>+</sup> and Br<sup>-</sup> and width of water-ion channels on different infinite plane gold surfaces. The standard error is given in small brackets. Values for Au(111), Au(110) and Au(100) are taken from<sup>15</sup>

Exposed surface	CTA <sup>+</sup> /nm <sup>2</sup>	Br <sup>-</sup> /nm <sup>2</sup>	channel width [nm]
Au (111)	1.31 (0.01)	1.09 (0.05)	0.94 (0.01)
Au(113)	1.58 (0.04)	1.53 (0.04)	0.28 (0.01)
Au(115)	1.51 (0.06)	1.60 (0.04)	0.43 (0.01)
Au(117)	1.59 (0.06)	1.61 (0.08)	0.41 (0.01)
Au(110)	1.49 (0.05)	1.41 (0.05)	0.71 (0.02)
Au(100)	1.49 (0.05)	1.40 (0.05)	0.73 (0.02)

The computed CTAB surface densities indicate that stepped surfaces can accommodate more CTAB molecules than flat surfaces, in line with the experimental observation of GNBs stabilization at high surfactant concentration. This is further supported by the widths of the inter-micelles channels obtained from MD simulations. As reported in Table 5, the water-ion channels on Au(113), Au(115) and Au(117) surfaces are 0.28, 0.43 and 0.41 nm, respec-

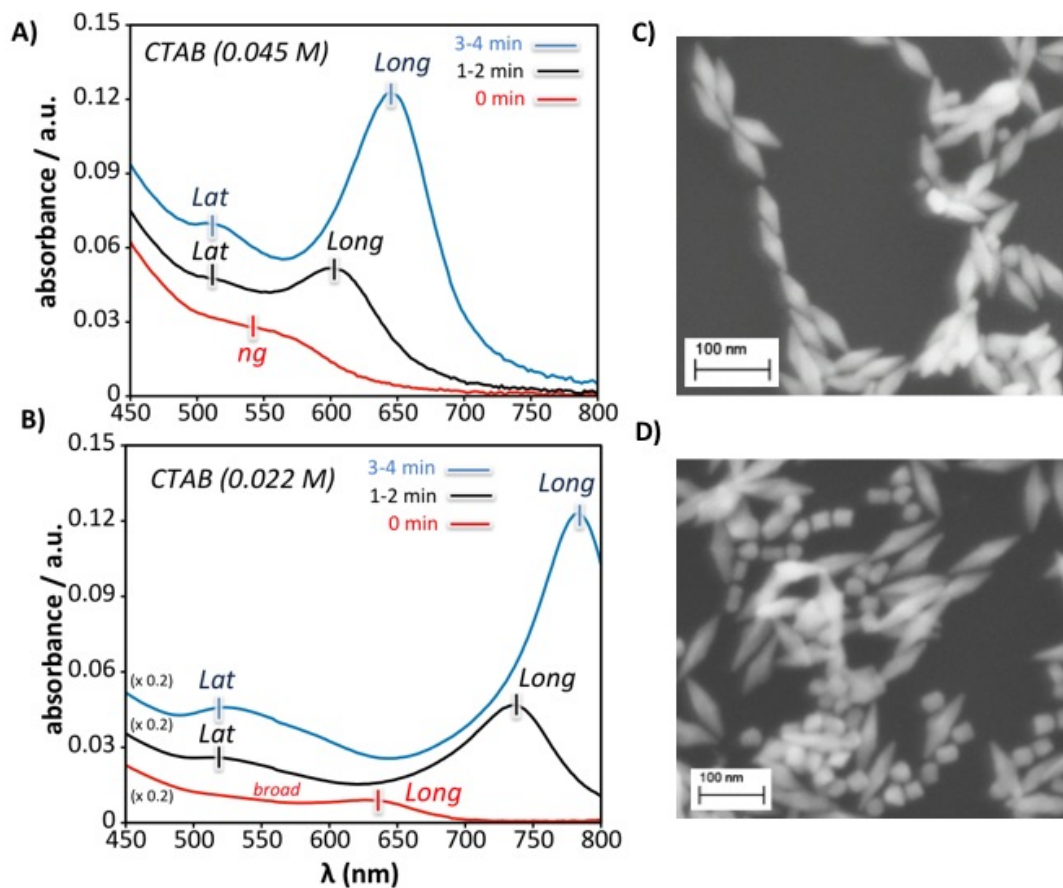


**Fig. 2** UV-vis spectra following the growth of the GNBs as function of CTAB concentration, namely (A) 0.045 M and (B) 0.022 M. Spectra are reported at the very early stages (few seconds, i.e. 0 min, red lines), at 1-2 min (black lines) and at 3-4 min (blue lines) after addition of gold seeds to the growth solution. Assignments of lateral (Lat), longitudinal (Long) and nanograins' (ng) LSPR bands are indicated.

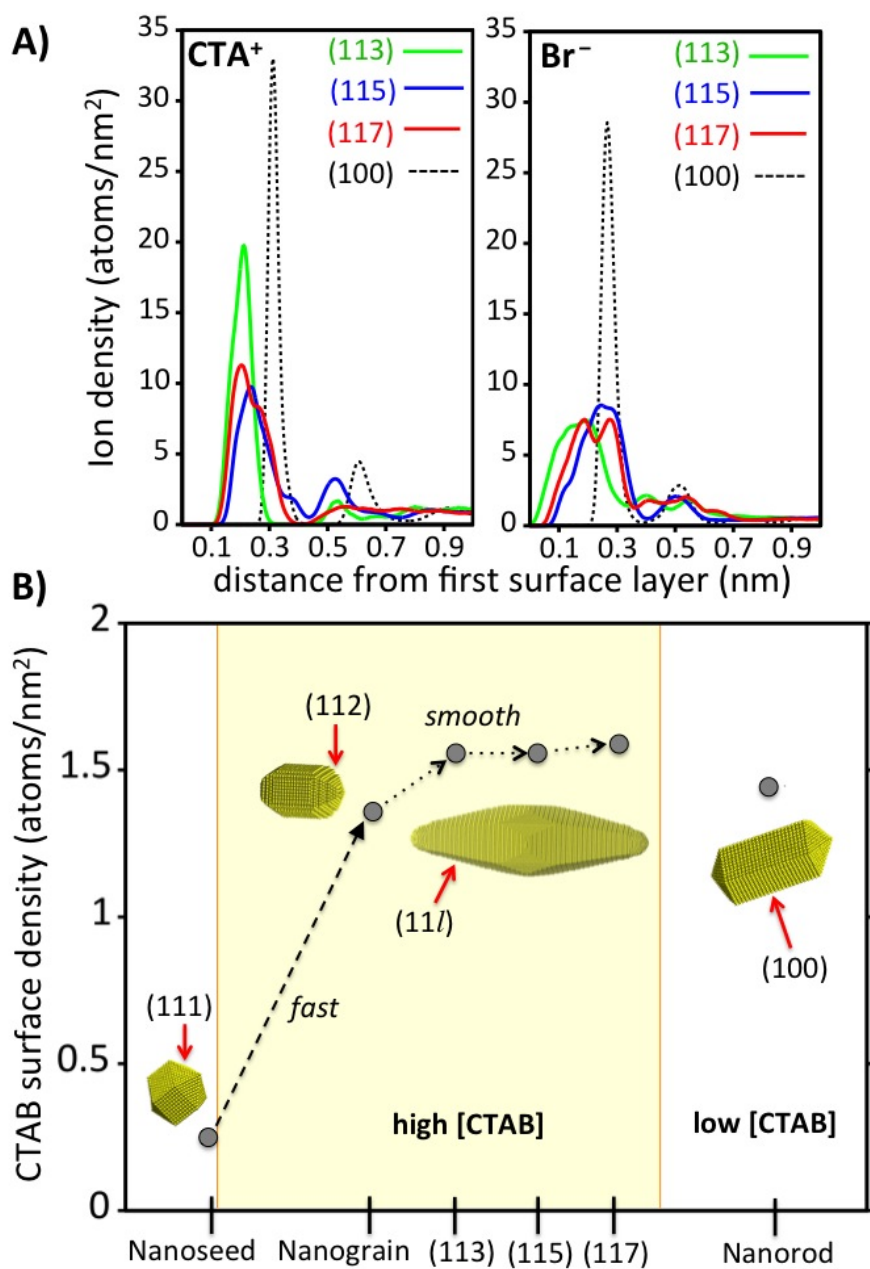


**Fig. 3** (A) CTA<sup>+</sup> and Br<sup>-</sup> ions density distribution on the lateral surfaces of GNBs, with (111) facets, and on nanorods, with Au(100) facets. Ions densities are reported as function of the distance (height) of ions from the first layer of the gold surface. (B) CTAB surface densities (computed as average densities of CTA<sup>+</sup> and Br<sup>-</sup> ions) on different exposed surfaces, showing different coverage of surfactant molecules between the (111) tips of penta-twinned seeds, the (112) bridges of nanograins, the (111) sides of GNBs and the (100) sides of nanorods.



tively, significantly narrower than those previously computed for lower-index surfaces, with Au(111), Au(110) and Au(100) featuring channels larger than 0.70 nm.<sup>16</sup> These results indicate that the diffusion of the AuCl<sub>2</sub><sup>−</sup> gold reactant towards the lateral facets of nano-bipyramids through the inter-micelles channels<sup>15</sup> would be significantly slowed down by the high surface density of the CTAB molecules and the compact arrangements of the micelles on the high-index (111) surfaces. Thus, as observed experimentally, providing enough CTAB molecules would favor a smooth, controlled growth of elongated bipyramidal objects that can be covered by more surfactants than the lateral (100) facets of nanorods.

The surface coverage of CTAB molecules on the stepped surfaces of GNBs is not only larger than that on flat surfaces but it also features a different arrangement of ions on top of the gold surfaces. As showed in Figure 3A, the density of CTA<sup>+</sup> and Br<sup>−</sup> ions as function of the distance from the gold surfaces indicates that the adsorption of ions on stepped Au(113), Au(115) and Au(117) surfaces clearly differs from that on the flat Au(100) surface. The ions density of Au(100) features the typical narrow double peaks at ~0.3 and ~0.6 nm,<sup>15</sup> while for high-index surfaces the two peaks are significantly broadened toward shorter distances from the first gold layer. This behaviour is due to the presence of surface steps that induce less homogeneous but still more dense distribution of ions on (111) than on (100) surfaces.

In Figure 3B, the trend of computed CTAB surface densities on different exposed surfaces are summarized. The dramatic change of surface density from the initial multi-twinned nanoseed with exposed (111) surfaces at the tip to the bridge facets of nanograins is associated with fast anisotropic growth even at high CTAB concentration. The large CTAB coverage found on the (112) bridges of nanograins explains the stability of these nano-objects at high surfactant concentrations and justify the observed smooth anisotropic growth toward more elongated GNBs with (111) side facets. We observed that the surfactant surface coverage on the exposed (100) surface of nanorods is lower than that on the GNBs sides, explaining why only when lowering the CTAB concentration nanorod-like objects are experimentally detected.

## 0.5 Conclusions

We have investigated the atomistic origin of controlled anisotropic growth of penta-twinned gold nanoseeds into nano-objects with bipyramidal geometry, possessing remarkable stability and relevant optical properties. Molecular dynamics simulations of realistic models of gold nanograins in solution with highly concentrated CTAB surfactant explained the formation of these stable nano-objects and elucidated their role as precursors for the smooth anisotropic growth of elongated GNBs with high-index 111 side facets. UV-vis electronic spectra monitoring the LSPR of growing gold nanoparticles and SEM images of the final nano-objects provided evidence of the fundamental role of CTAB concentration for controlling the monodispersity and the growth kinetics of the GNBs synthesis. In fact, maintaining high surfactant concentration in the growth solution avoids fast and uncontrolled growth that would give rise to undesired formation of small nanorods with (100) side facets. The theoretical results clearly indicate that the surface coverage of CTAB surfactant molecules and the width of inter-micelles channels significantly depends on the exposed surfaces. High-index Au(113), Au(115) and Au(117) stepped surfaces of GNBs showed higher CTAB coverage and narrower inter-micelles channels than flat (100) surface, in agreement with the experimentally observed smooth growth of the bipyramidal objects and their preferential formation over nanorods at high surfactant concentra-

tions. The total ion density found to be increased on all the facets due to the addition of silver ions and anisotropic coverage of silver ions together with anisotropic coverage of CTA<sup>+</sup> and Br<sup>−</sup> ions with higher surface densities on the different facets of nanograin as compare to the absence of silver ions lead to controlled anisotropic growth of nanobypiramids. Finally, the combined theoretical and experimental data support the following anisotropic growth mechanism of monodisperse gold bipyramids: at high CTAB concentrations, the initial penta-twinned seeds are rapidly converted into nanograins that are largely covered at their Au(100) sides and Au(112) bridge facets, while their Au(111) and Au(110) tips are exposed to the gold reactant; the highly covered Au(112) bridges ensure that further anisotropic growth of nanograins proceeds by reducing the cone angle of the nanoparticles, yielding higher index facets such Au(113), Au(115) and Au(117) that progressively and smoothly appear as stepped surfaces on the GNBs sides; these stepped surfaces are highly covered by CTAB micelles and results to be quite stable, with rather narrow inter-micelles channels that hamper the access of gold reactants to the surface, slowing down the growth kinetics and hampering further growth toward the Au(100) flat surfaces of nanorods. If the surfactant concentration is low, instead, only part of the penta-twinned seeds undergoes this smooth growth and converts into GNBs while the remaining seeds would lack enough CTAB coverage to smoothly generate high-index 111 side facets thus forming nanorods or spheres. This outcome, thus, elucidates the role of surfactant concentration on the stabilization of gold stepped surfaces that preferentially forms during the smooth anisotropic growth of gold nano-bipyramids.

## Conflicts of interest

“There are no conflicts to declare”.

## Acknowledgements

IR, MS and SKM gratefully acknowledge the use of HPC resources of the “Pôle Scientifique de Modélisation Numérique” (PSMN) of the ENS-Lyon, France, “Mogon ZDV” of Johannes Gutenberg University Mainz, Germany and computational facilities at Chemical Engineering and Process Development Division, CSIR-National Chemical Laboratory (NCL), Pune, India. M.Sulpizi acknowledges the Deutsche Forschungsgemeinschaft (DFG) SFB TRR 146 (project A4). S. K. Meena acknowledges CSIR-NCL project grant no. MLP036726. We thank the ENS Lyon and the LABEX iMUST (ANR-10-LABX-0064) of the Université de Lyon for financial support.

## References

- 1 H. Zhang, Z. She, H. Su, K. Kerman and H. Kraatz, *Analyst*, 2016, **141**, 6080–6086.
- 2 M. Liu and P. Guyot-Sionnest, *Phys. Rev. B*, 2007, **76**, 235428.
- 3 M. Liu and P. Guyot-Sionnest, *J. Phys. Chem. B*, 2005, **109**, 22192–22200.
- 4 G. Zhou, Y. Yang, S. Han, W. Chen†, Y. Fu, C. Zou†, L. Zhang and S. Huang, *ACS Appl. Mater. Interfaces*, 2013, **5** (24), 13340–13352.
- 5 Z. C. Canbek, R. Cortes-Huerto, F. Testard, O. Spalla, S. Moldovan, O. Ersen, A. Wisnet, G. Wang, J. Goniakowski, C. Noguera and N. Menguy, *Cryst. Growth Des.*, 2015, **15** (8), 3637–3644.
- 6 J.-H. Lee, K. J. Gibson, G. Chen and Y. Weizmann, *Nat. Commun.*, 2015, **6**, 7571.
- 7 N. K. Geitner, A. Doepeke, M. A. Fickenscher, J. M. Yarrison-Rice,

- W. R. Heineman, H. E. Jackson and L. M. Smith, *Nanotechnology*, 2011, **22**, 275607.
- 8 D. Chateau, A. Liotta, F. Vadcarg, J. R. G. Navarro, F. Chaput, J. Lerne, F. Lerouge and S. Parola, *Nanoscale*, 2015, **7**, 1934–1943.
  - 9 D. Chateau, A. Desert, F. Lerouge, G. Landaburu, S. Santucci and S. Parola, *ACS Appl. Mater. Interfaces*, 2019, **11** (42), 39068–39076.
  - 10 J. R. G. Navarro, D. Manchon, F. Lerouge<sup>1</sup>, E. Cottancin, J. Lermé, C. Bonnet, F. Chaput, A. Mosset, M. Pellarin and S. Parola, *Nanotechnology*, 2012, **23**, 14570.
  - 11 J. Burgin, I. Florea, J. Majimel, A. Dobri, O. Ersen and M. Treguer-Delapierre, *Nanoscale*, 2012, **4**, 1299–1303.
  - 12 H. Yoo and M. H. Jang, *Nanoscale*, 2013, **5**, 6708–6712.
  - 13 G. González-Rubio, L. Scarabelli, A. Guerrero-Martínez and L. M. Liz-Marzán, *ChemNanoMat*, 2020, **6**, 698–707.
  - 14 N. Almora-Barrios, G. Novell-Leruth, P. Whiting, L. M. Liz-Marzán and N. López, *Nano Lett.*, 2014, **14** (2), 871–875.
  - 15 S. K. Meena and M. Sulpizi, *Langmuir*, 2013, **29** (48), 14954–14961.
  - 16 S. K. Meena and M. Sulpizi, *Angew. Chem. Int. Ed.*, 2016, **55** (39), 11960–11964.
  - 17 S. K. Meena, S. Celiksoy, P. Schafer, A. Henkel, C. Sonnichsen and M. Sulpizi, *Phys. Chem. Chem. Phys.*, 2016, **18** (19), 13246–13254.
  - 18 H. Heinz, K. Jha, J. Luettmer-Strathmann, R. A. Farmer and R. R. Naik, *J. R. Soc. Interface*, 2011, **8**, 220–232.
  - 19 I. L. Geada, H. Ramezani-Dakhel, T. Jamil, M. Sulpizi and H. Heinz, *Nat. Commun.*, 2018, **9**, 716.
  - 20 H. J. C. Berendsen, D. van der Spoel and R. van Drunen, *Comput. Phys. Commun.*, 1995, **91**, 43–56.
  - 21 D. V. D. Spoel, E. Lindahl, B. Hess, G. Groenhof, A. E. Mark and H. J. C. Berendsen, *J. Comput. Chem.*, 2005, **26**, 1701–1718.
  - 22 B. Hess, C. Kutzner, D. V. D. Spoel and E. Lindahl, *J. Chem. Theory Comput.*, 2008, **4**, 435–447.
  - 23 S. Pronk, S. Pall, R. Schulz, P. Larsson, P. Bjelkmar, R. Apostolov, M. R. Shirts, J. C. Smith, P. M. Kasson, D. van der Spoel, B. Hess, and E. Lindahl, *Bioinformatics*, 2013, **29**, 845–854.
  - 24 C. Oostenbrink, A. Villa, A. E. Mark and W. F. V. Gunsteren, *J. Comput. Chem.*, 2004, **25**, 1656–1676.
  - 25 Z. Wang and R. G. Larson, *J. Phys. Chem. B.*, 113, **2009**, 13697–13710.
  - 26 H. Yu, M. Ramseier, R. Burgi and W. F. van Gunsteren, *ChemPhysChem*, 2004, **5**(5), 633–641.
  - 27 H. Heinz, R. A. Farmer and R. R. Naik, *J. Phys. Chem. B.*, 112, **2008**, 17281–17290.